Mesomorphism of Imidazolium-based Fluorinated Ionic Liquids

Randinu Pulukkody¹, Yoo Jin Lee², Taylor H. Ware^{2,3} and Emily B. Pentzer^{1,3,*}

¹Department of Chemistry, Texas A&M University, College Station, TX 77843

²Department of Biomedical Engineering, Texas A&M University, College Station, TX, 77843

³Department of Materials Science and Engineering, Texas A&M University, College Station, TX, 77843

**emilypentzer@tamu.edu*

Abstract

lonic liquid crystals have received increasing interest due to their positional and/or orientational order as well as the freedom in molecular motions that arise from the formation of mesophases between solid and liquid. While phase changes of non-fluorinated ionic liquids have been widely reported, there have been few reports on the temperature-dependent phase behavior of fluorinated ionic liquids. Here, we present a series of fluorinated ionic liquids with methylimidazolium cations bearing 1H, 1H, 2H, 2H-perfluoroalkyl chains (butyl, hexyl, and octyl) and halide counterions, and demonstrate their thermotropic mesomorphism. These cations were synthesized under solvent-free conditions, and anion exchange was used to vary the halide counterion. The thermal stability of the compounds was studied using thermogravimetric analysis and differential scanning calorimetry revealed both liquid crystalline phases and solid-solid transitions. We discovered that the mesomorphic properties of the ionic liquids depend strongly on the length of the polyfluoroalkyl pendants. Specifically, ionic liquids with a fluorinated butyl chain showed no mesophase behavior while those with hexyl and octyl fluorinated chains displayed liquid crystalline phases at temperatures above 100 °C. The mesophases were further characterized by polarized optical microscopy and powder X-ray diffraction, highlighting the impact of the fluorinated alkyl chain length.

1. Introduction

lonic liquids (ILs) have emerged as a new class of compounds, applicable in a variety of fields including carbon dioxide capture and storage, reaction media for catalysis, thermal energy storage, and biomedicine. This wide range of applications is supported by their favorable physicochemical properties such as high thermal stability, non-flammability, low volatility, and high ionic conductivity. These properties can be tuned by tailoring cation-anion pairs to introduce chemical features for desired applications. For example, the introduction of certain pendant groups such as alkyl chains onto the cation of an IL can induce the formation of mesophases intermediate to solid and liquid phases, thus generating ionic liquid crystals (ILCs). Liquid crystal (LCs) mesophases possess positional and/or orientational order as well as freedom in molecular motions. ILCs can combine the desirable properties of traditional ILs with those of LCs, such as fluidity and structural anisotropy, to afford advanced materials for electrochemical applications.

ILCs have been widely explored for applications ranging from ion-conducting membranes, to separation membranes, to host framework for guest binding, to optoelectronic materials. ^{15,17–20} For example, Yamanaka *et al.* reported the use of imidazolium-based ILCs as electrolytes in a dye-sensitized solar cell (DSSC); the high ionic conductivity of the ILC resulted in high short-circuit current densities and high power conversion efficiencies. ²¹ A common strategy for designing ILC compounds is to introduce long alkyl chains to the anion or cation of an IL. ²² Indeed, using an appropriate alkyl chain length allows for phase separation of nonpolar and polar moieties, facilitating the formation of liquid crystalline phase(s). ^{15,16,22,23} For instance, Bowlas and coworkers show that 1-alkyl-3-methylimidazolium iodide salts with alkyl chains containing at least eleven carbon atoms exhibited liquid crystalline smectic A (SmA) phases. ¹⁵

Fluorinated ILs and fluorinated ILCs are a relatively underexplored class of soft matter. We define fluorinated ILs as those comprising an anion and/or cation with fluorinated alkyl or aryl groups containing four or more

carbon atoms. Compared to their non-fluorinated derivatives, fluorinated ILs have the ability to form fluorophilic domains—in addition to polar and nonpolar domains—which makes them ideal candidates for tailored applications such as solvation of greenhouse gases, recovery of perfluorocarbon contaminants, and electrolytes in energy storage devices. Abate and coworkers showed that DSSC electrolytes containing fluorinated imidazolium-based ILs outperform their hydrogenated counterparts due to superior regeneration efficiency and charge transport rate. The benefits of fluorination can be extended to ILCs; the same authors demonstrated the anisotropic ionic conductivity in a smectic A liquid crystalline phase of the fluorinated IL, stable over the operational temperature range of common photovoltaic devices (44-106 °C). Tailoring the chemical composition of fluorinated ILCs offers ample opportunities for tuning the thermotropic phase behavior for this intriguing, and understudied, class of materials for a variety of potential applications.

Scheme 1. General molecular structure of the fluorinated ILs prepared and studied in this work.

Herein, we report the synthesis and mesophase characterization of nine fluorinated ILs consisting of iodide, bromide, and chloride anions and methylimidazolium-based cations with fluoroalkyl butyl, hexyl, and octyl chains. **Scheme 1** shows the general structure of these fluorinated ILs and naming scheme used throughout. In each fluorinated IL, one nitrogen atom of the imidazolium core bears a methyl group while the other carries a fluorinated alkyl chain of varying length (including two methylene spacer units). We demonstrate that ILs with hexyl and octyl fluorinated alkyl chains exhibit mesomorphism as confirmed through differential scanning calorimetry (DSC), polarized optical microscopy (POM), and variable temperature powder X-ray diffraction (PXRD), whereas ILs with butyl fluoroalkyl chains only displayed polymorphic behavior. These findings suggest the existence of a threshold fluorinated alkyl chain length above which the ILs exhibit mesomorphic behavior, providing insight into the molecular design of IL-based electrolytes.

2. Experimental Section

2.1 Materials

All chemicals were purchased from commercial sources and used directly as received, unless otherwise stated. *N*-methylimidazole (99%), isopropanol, 1H, 1H, 2H, 2H-perfluorooctyl iodide (97%) and 1H, 1H, 2H, 2H-perfluorohexyl iodide (97%) were purchased from Fisher Scientific. 1H, 1H, 2H, 2H-perfluorodecyl iodide (96%), ammonium chloride (99.5%), ammonium bromide (99%), and methanol (99.8%) were purchased from Sigma Aldrich.

2.2 Instrumentation

Chemical composition and purity characterization: ¹H and ¹⁹F nuclear magnetic resonance (NMR) spectroscopy was carried out using a Bruker Avance NEO 400 MHz NMR spectrometer using CD₂Cl₂

(dichloromethane-d₂) as the solvent. Purity of compounds was determined *via* C, H, N, F elemental analysis performed at Atlantic Microlabs. Each IL was dried under vacuum for 24 h at 50 °C prior to characterization.

Thermal characterization: Thermogravimetric analysis (TGA) was recorded on a TA Instruments TGA 5500 under N_2 gas. Each sample was heated to 100 °C, equilibrated for 5 min, and ramped to 450 °C at 10 °C/min. Differential scanning calorimetry (DSC) was carried out on a TA instruments DSC 2500 using aluminum pans. DSC samples were prepared in a glovebox to limit exposure to moisture. The samples were then cooled to -80 °C at 10 °C/min, equilibrated for 1 min and ramped 10 °C/min to the highest temperature for each sample— approximately 50 °C less than the 5% mass loss temperature ($T_{5\%}$), as determined using TGA. Three cooling-heating cycles were collected for each sample (second and third heating cooling cycles reported).

Optical microscopy: Polarized optical microscopy (POM) images were recorded on a Nikon Eclipse optical microscope (LV100N POL) to observe the phase behavior of each sample, where the temperature was controlled using a Linkam thermal stage. For POM analysis, the IL was inserted into a glass cell. To prepare the glass cells, the glass slides were first cleaned in an aqueous Alconox solution, then sprayed with acetone followed by isopropanol and dried in air. The slides were then plasma treated to impart hydrophilicity and coated with PVA solution (1wt% in deionized water) using a spin coater. The spin coater was operated at a speed of 2300 rpm for 30 seconds to deposit 0.5 mL of solution. The coated glass slides were then directly assembled to produce a glass cell with a 45 μm gap. For images at cold temperatures, the samples were stored in a refrigerator at 7 °C overnight and characterized by POM immediately after removal.

Crystallography: Powder X-ray diffraction (PXRD) patterns were collected on a Bruker D8 Discover diffractometer at 40 kV, 40 mA with CuK α (λ : 1.54056 Å) radiation. A thermally controlled stage was utilized to record XRD patterns at various temperatures at which phase changes occur for each IL, guided by DSC data.

2.3 Methods

Synthesis of iodide salts: A modified literature procedure³¹ was used for the synthesis of [(EtPFBut)Melm][I], [(EtPFHex)Melm][I], [(EtPFOct)Melm][I]. In a nitrogen filled glovebox, 1-methylimidazole (12.5 mmol, 1 eq) was combined with the appropriate 1H, 1H, 2H, 2H-perfluoroalkyl iodide (18.8 mmol, 1.5 eq) in a Schlenk flask. The reaction flask was then taken out of the glovebox, equipped with an air condenser, connected to the Schlenk line, and degassed by three consecutive freeze-pump-thaw cycles. The reaction mixture was placed under nitrogen and heated to 120 °C for 6 h, after which a yellow solid was observed along with a clear liquid layer. The ¹H NMR spectrum of the crude mixture (containing both the solid and liquid layer) revealed the presence of the target compound along with by-products from Hofmann elimination: N-methylimidazolium iodide and 1H, 1H, 2H-perfluoro-1-octene. The liquid layer containing unreacted 1H, 1H, 2H, 2H-perfluoroalkyl iodide and 1H, 1H, 2H-perfluoro-1-octene, was removed by pipet. The solid was then washed with diethyl ether and dried under vacuum at 50 °C. The ¹H NMR spectrum of the yellow solid showed the presence of the desired [(EtPFAlkyl)Melm][I] as well as the elimination by-product, N-methylimidazolium iodide. To remove this byproduct, the crude product was dissolved in a minimal amount of acetonitrile, loaded onto a neutral alumina column (packed using toluene), and the column was washed with excess acetonitrile. The eluent was collected and concentrated at 50 °C to remove acetonitrile and toluene followed by freeze drying overnight to afford pure [(EtPFAlkyl)Melm][I] as a dark yellow solid product.

[(EtPFBut)MeIm][I] was synthesized from 1-methylimidazole and 1H, 1H, 2H, 2H-perfluorohexyl iodide. Yellow solid 2.5 g, 45%). 1 H NMR (400 MHz, CD₂Cl₂-d₂) δ 2.98 (m, 2H), 4.03 (s, 3H), 4.82 (t, 2H), 7.46 (s, 1H), 7.66 (s, 1H), 10.20 (s, 1H). 19 F NMR (376 MHz, CD₂Cl₂-d₂) δ -81.41, -113.90, -124.40, -126.24.

[(EtPF**Hex**)MeIm][I] was synthesized from 1-methylimidazole and 1H, 1H, 2H, 2H-perfluorooctyl iodide. Yellow solid (6.3 g, 69%). 1 H NMR (400 MHz, CD₂Cl₂-d₂) δ 2.98 (m, 2H), 4.04 (s, 3H), 4.82 (t, 2H), 7.36 (s,

1H), 7.53 (s, 1H), 10.24 (s, 1H). ^{19}F NMR (470 MHz, $CD_2CI_2-d_2$) δ -81.18, -113.63, -122.03, -123.07, -123.40, -126.39.

[(EtPFOct)MeIm][I] was synthesized from 1-methylimidazole and 1H, 1H, 2H, 2H-perfluorodecyl iodide. Yellow solid (3.5 g, 48%). 1 H NMR (400 MHz, CD₂Cl₂-d₂) δ 2.97 (m, 2H), 4.03 (s, 3H), 4.83 (t, 2H), 7.26 (s, 1H), 7.41 (s, 1H), 10.43 (s, 1H). 19 F NMR (470 MHz, CD₂Cl₂-d₂) δ -81.12, -113.54, -121.76, -122.05, -122.89, -123.33, -126.33.

Synthesis of chloride and bromide salts: A modified literature procedure³² was used for the preparation of chloride and bromide salts via anion exchange of the prepared iodide salts ([(EtPFAlkyl)Melm][I]). A glass column with 0.5-inch inner diameter and 18-inch height was packed with 7.5 g of the strongly basic anion exchange resin, Amberlyst A-26, and washed with water. The column was then treated with a 1% (w/v%) solution of the appropriate ammonium halide in a water/methanol mixture; ammonium chloride was used to prepare the chloride salt and ammonium bromide was used to prepare the bromide salt. This solution was passed through the resin until the pH of the eluant reached the same pH as the original 1% solution and remained constant. The column bed was then washed with water/methanol mixtures having progressively higher percentages of methanol, up to 100% methanol. A solution of the imidazolium iodide salt (1.8 mmol) in 30 mL of methanol was then passed through the column (gravity elution) and the column was then flushed with 75 mL of methanol. The combined eluates were concentrated and dried at 50 °C overnight to afford an off-white solid powder.

[(EtPFBut)MeIm][CI]. Off-white solid. 1 H NMR (400 MHz, CD₂Cl₂-d₂) δ 3.01 (m, 2H), 4.02 (s, 3H), 4.85 (t, 2H), 7.42 (s, 1H), 7.72 (s, 1H), 11.12 (s, 1H). 19 F NMR (470 MHz, CD₂Cl₂-d₂) δ -81.42, -114.00, -124.46, -126.25.

[(EtPFHex)MeIm][CI]. Off-white solid. 1 H NMR (400 MHz, CD₂Cl₂-d₂) δ 3.01 (m, 2H), 4.02 (s, 3H), 4.86 (t, 2H), 7.43 (s, 1H), 7.73 (s, 1H), 11.14 (s, 1H). 19 F NMR (470 MHz, CD₂Cl₂-d₂) δ -81.25, -113.81, -122.12, 123.14, -123.52, -126.46.

[(EtPFOct)MeIm][CI]. Off-white solid. 1 H NMR (400 MHz, CD₂Cl₂-d₂) δ 3.00 (m, 2H), 4.02 (s, 3H), 4.85 (t, 2H), 7.21 (s, 1H), 7.37 (s, 1H), 11.29 (s, 1H). 19 F NMR (470 MHz, CD₂Cl₂-d₂) δ -81.12, -113.57, -121.78, -122.06, -122.89, -123.38, -126.32.

[(EtPFBut)MeIm][Br]. White solid. ¹H NMR (400 MHz, CD₂Cl₂-d₂) δ 3.00 (m, 2H), 4.03 (s, 3H), 4.85 (t, 2H), 7.42 (s, 1H), 7.65 (s, 1H), 10.73 (s, 1H). ¹⁹F NMR (470 MHz, CD₂Cl₂-d₂) δ -81.40, -113.94, -124.43, -126.23.

[(EtPF**Hex**)MeIm][Br]. White solid. 1 H NMR (400 MHz, CD₂Cl₂-d₂) δ 3.00 (m, 2H), 4.03 (s, 3H), 4.86 (t, 2H), 7.50 (s, 1H), 7.77 (s, 1H), 10.64 (s, 1H). 19 F NMR (470 MHz, CD₂Cl₂-d₂) δ -81.30, -113.83, -122.14, -123.15, -123.52, -126.50.

[(EtPFOct)MeIm][Br]. Dark yellow solid. 1 H NMR (400 MHz, CD₂Cl₂-d₂) δ 2.99 (m, 2H), 4.03 (s, 3H), 4.86 (t, 2H), 7.23 (s, 1H), 7.39 (s, 1H), 10.99 (s, 1H). 19 F NMR (470 MHz, CD₂Cl₂-d₂) δ -81.12, -113.55, -121.77, -122.06, -122.93, -123.37, -126.31.

3. Results and Discussion

3.1 Design and synthesis of the ILs

The general formula of the fluorinated imidazolium-based ILs discussed in this work are shown in **Scheme 1** and can be represented as [(EtPFAlkyl)Melm][X]. ILs of cations containing butyl-([(EtPFBut)Melm]), hexyl-([(EtPFHex)Melm]), and octyl-([(EtPFOct)Melm]) fluorinated alkyl chains with halide anions Cl⁻, Br⁻ and l⁻ were prepared, giving a small matrix of nine different fluorinated ILs. These chemistries were selected to

systematically investigate the effects of (i) fluorinated alkyl chain length and (ii) halide anion on mesomorphic behavior of the ILs. The iodide salts were synthesized via a neat reaction between methylimidazole and the corresponding 1H, 1H, 2H, 2H- perfluoroalkyl iodide (see experimental for details). For instance, [(EtPFHex)Melm][I] was synthesized by reacting 1H, 1H, 2H, 2H- perfluorohexyl iodide with methylimidazole. The chloride and bromide salts were prepared through anion exchange of the iodide salts using a basic resin, and ¹H NMR spectroscopy, along with elemental analysis, confirmed successful anion exchange and purity. As demonstrated in the ¹H NMR spectra in **Fig. 1**, the shielding environment of the imidazolium C2-H varies with the nature of the anion: C2-H chemical shifts in CD₂Cl₂-d₂ are 11.12 ppm for [(EtPFHex)Im][CI], 10.64 ppm for [(EtPFHex)Im][Br], and 10.24 ppm for [(EtPFHex)Im][I]. The difference in these values can be attributed to the varying hydrogen bond strength between C2-H and the anion. The coordinating ability of the anions follows the trend of I- < Br- < CI-, with CI- exhibiting the highest hydrogen bond accepting capability, leading to a more pronounced downfield shift in the resonance of C2-H within the cation. **Table S1** summarizes the chemical shifts of the C2-H for the nine imidazolium salts as well as their purity, as determined by elemental analysis (all > 99.6%).

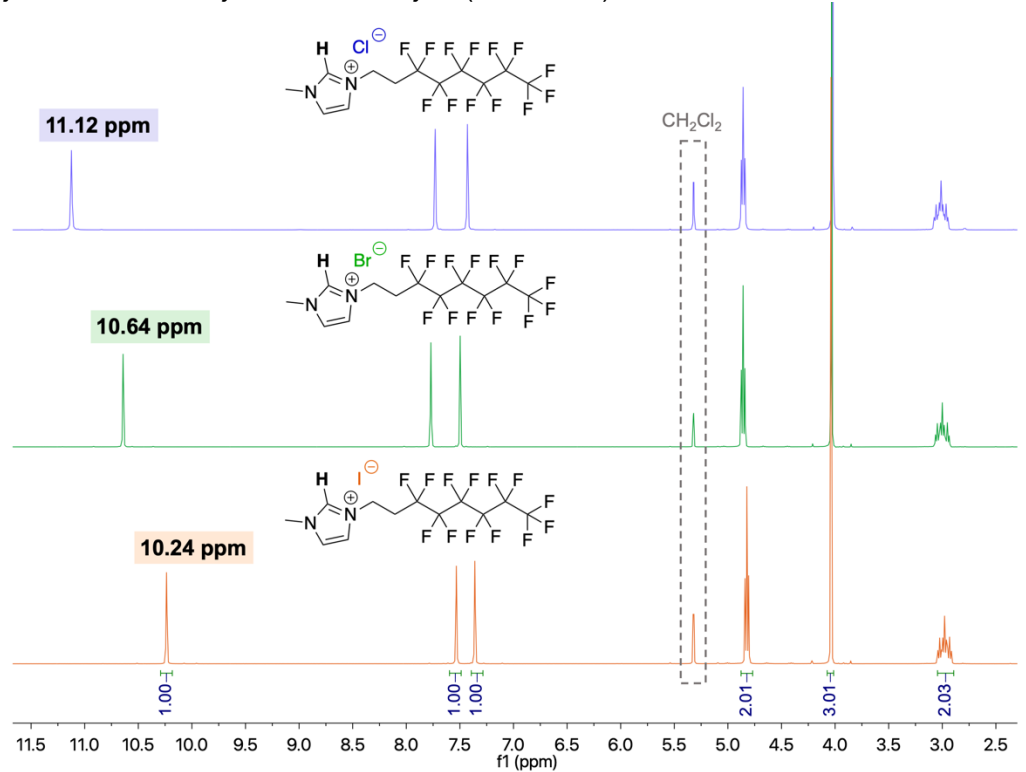


Fig. 1 ¹H NMR spectra of [(EtPFHex)Im][I] (orange), [(EtPFHex)Im][Br] (green), [(EtPFHex)Im][CI] (blue), illustrating the difference in chemical shift (and thus local environment) of the C2 proton, dependent on anion identity. All spectra were taken in DMSO-d6 (which contained water).

3.2 Thermal Stability of the ILs via TGA

The thermal stability of the three [(EtPFHex)MeIm][X] salts was first investigated using thermogravimetric analysis (TGA). To do so, the compound was first heated from room temperature to 100 °C and held isothermally for 5 minutes, then heated from 100 °C to 450 °C at a ramp rate of 10 °C/min. The thermograms shown in **Fig. 2** illustrate that all samples exhibit significant mass loss above 240 °C, and no further weight loss above 300 °C. The 5% mass loss temperatures ($T_{5\%}$) for [(EtPFHex)Im][CI], [(EtPFHex)Im][Br] and [(EtPFHex)Im][I] salts were 226 °C, 237 °C and 234 °C, respectively; the first derivatives of the weight loss profiles illustrate that only small differences in thermal stability (e.g., minor decomposition steps) are apparent (**Fig. S1**). In addition to these ILs, the thermal stability of [(EtPFBut)Im] (**Fig. S2**) and [(EtPFOct)Im] (**Fig. S3**) ILs were also studied. The $T_{5\%}$ values for [(EtPFBut)Im][CI], [(EtPFBut)Im][Br] and [(EtPFBut)Im][I]

were 230 °C, 244 °C and 237 °C, respectively, while ILs with [(EtPFOct)Im] cations displayed 5% mass loss temperatures of 224 °C, 235 °C and 233 °C for chloride, bromide, and iodide salts, respectively. Thus, neither the length of the fluorinated alkyl chain of the cation nor identity of the anion has a significant impact on the $T_{5\%}$.

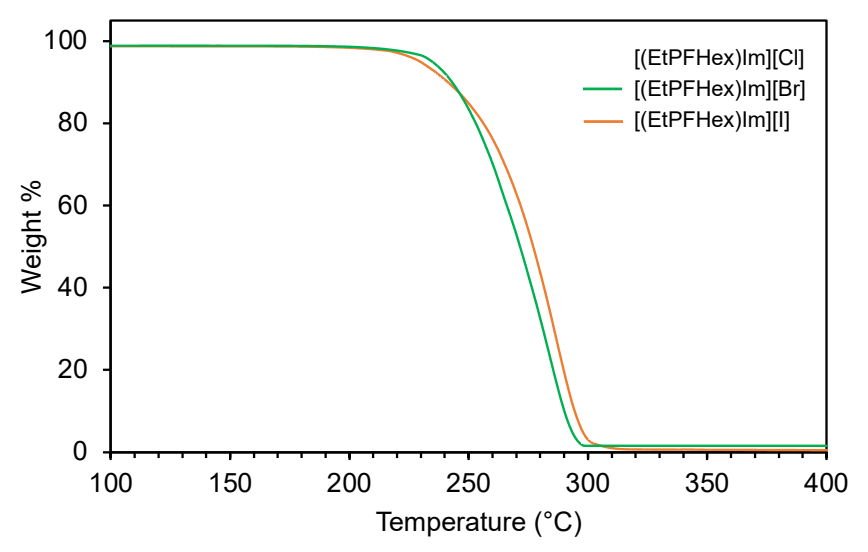


Fig. 2 TGA weight loss profiles of [(EtPFHex)Im][X] where X = CI, Br, or I.

3.3 Thermal Characterization of ILs via DSC and PXRD.

To evaluate the thermal phase transitions of these ILs, differential scanning calorimetry (DSC) was performed from -80 °C to a maximum temperature that is \sim 50 °C below $T_{5\%}$ for each IL. For each sample, an initial heating and cooling cycle was performed to erase the thermal history, followed by two additional cycles which were consistent with each other. **Fig. 3** depicts the heating thermograms of the iodide salts containing cations with fluorinated hexyl, octyl, and decyl chains (second cycle). In complement, powder X-ray diffraction (PXRD) spectra were collected on an open-air heating stage across the same temperature ranges. As with DSC, for PXRD, the sample was first heated until isotropic then cooled to room temperature to erase the thermal history and data was collected during the second heating cycle. In **Fig.3**, the arrows on the DSC thermogram are color coded to the different temperatures in the PXRD spectra. **Table S2** summarizes all phase transitions and temperatures for the nine ILs.

3.3.1 Salts containing [(EtPFBut)Im] cation with fluorinated butyl chains. In the DSC thermogram for [(EtPFBut)Im][I] (Fig. 3a(i), Fig. S4), upon heating from -80 °C, first, a glass transition is observed at -15 °C, followed by an exothermic peak at 9 °C (cold crystallization), an endothermic peak at 61 °C (solid-solid transition), and then a larger enthalpic peak at 70 °C (melting to isotropic). As such, at 24 °C, a crystalline solid is expected, as supported by the PXRD pattern which shows three main reflections at 15°, 22° and 23° 20 (blue trace in Fig. 3a(ii)). As the temperature increases to 60 °C, the same XRD pattern persisted but with decreased intensities of the three main Bragg peaks. Continued heating above 75 °C led to disappearance of the peaks at 15°, 22° and 23° 20 and appearance of new peaks at 17°, 20° and 25° 20, which increased in intensity as the temperature approached 85 °C, suggesting completion of the solid-solid phase transition. Again, consistent with DSC data, above ~100 °C, the XRD data is featureless barring a broad amorphous halo, indicating an isotropic system (e.g., liquid). Notably, the temperature for phase changes observed in the XRD occur at slightly higher temperatures than observed for DSC; this offset might be caused by a temperature gradient between the sample and the heating stage, resulting in overestimation of the sample temperature. The anion of the salt had little impact on thermal transitions: the DSC thermogram of [(EtPFBut)Im][Br] shows a similar pattern with a large endothermic peak at 66 °C, indicating melting, and an exothermic cold crystallization peak at 47 °C along with a glass transition at -9 °C (Fig. S5). In a similar vein, [(EtPFBut)Im][CI] displays a large endothermic peak for melting at 77 °C, a cold

crystallization peak at 54 °C and a glass transition at -2 °C on the DSC thermogram (**Fig. S6**). No other phase transition peaks were visible. All three of these salts with the [(EtPFBut)Im] cation did not exhibit any mesomorphic properties (detailed later).

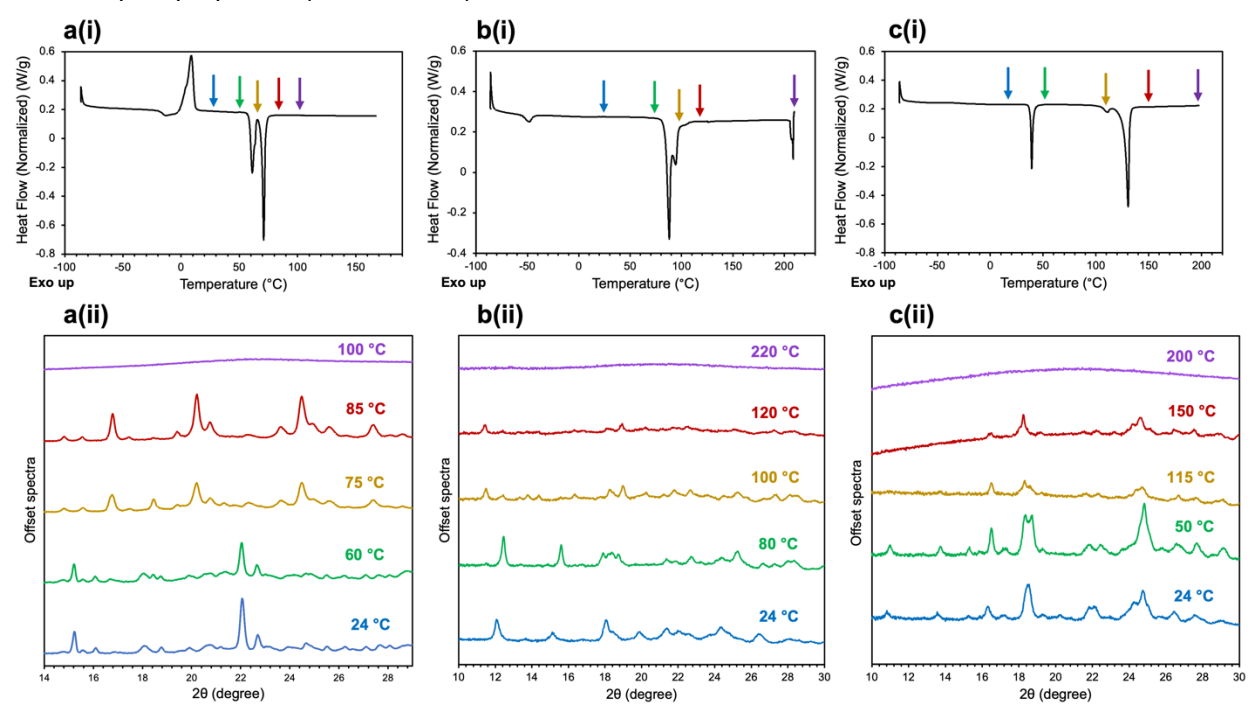


Fig. 3 Second heating cycle for DSC (top) and powder XRD patterns (bottom) for (a) [(EtPFBut)Im][I], (b) [(EtPFHex)Im][I], and (c) [(EtPFOct)Im][I].

3.3.2 Salts containing [(EtPFHex)Im] cations with fluorinated hexyl chains. The DSC thermogram of [(EtPFHex)Im][I] (Fig. 3b(i), Fig. S7), upon heating, displays a glass transition peak with enthalpic relaxation at -50 °C, followed by a large endothermic peak at 88 °C (melting). The additional peak observed at 210 °C was identified as the clearing temperature (Tc), suggesting the presence of a liquid crystalline phase from 88-210 °C. The XRD pattern of this compound at 24° C features sharp reflections at 12°, 15°, 18° and 27° 20 characteristic of a crystalline phase of [(EtPFHex)Im][I] (Fig. 3b(ii)). Upon heating to 80 °C, the diffraction pattern begins to change, consistent with melting, as observed in the DSC thermogram. At 100 °C, the diffractogram shows no sharp reflections (yellow PXRD pattern in Fig. 3b(ii)) but reveals the emergence of new peaks at 11° and 19° 20 indicative of a possible liquid crystalline phase. Previous reports have associated features at higher 20 values with increased positional order of molecules within the smectic layer.33 Further heating of the sample results in the disappearance of all sharp features, giving way to a featureless diffraction pattern at around 220 °C. Contrary to the results from the previous set of ILs, the anion of the fluorinated hexyl imidazolium salt impacts the thermal behavior; the DSC of [(EtPFHex)Im][Br] displayed three endothermic peaks with the largest representing melting at 115 °C (Fig. S8). The two peaks before the T_m at 92 °C and 99 °C suggest solid-solid phase transitions, which can be characterized further through XRD, although this aspect is not addressed in this study. No Tc peak was observed for this IL up to 185 °C, and the sample was not heated further to avoid decomposition. The [(EtPFHex)Im][CI] DSC thermogram (Fig. S9) shows a glass transition occurring at -60 °C along with a solid-solid phase transition at 82 °C. The broader peak at 105 °C can be identified as T_m, with confirmation of this assignment provided by POM (see below). A T_c peak is also clearly visible at 205 °C for this salt.

3.3.3 Salts containing [(EtPFOct)Im] cations with fluorinated octyl chains. In the DSC thermogram of [(EtPFOct)Im][I] (**Fig. 3c(i), Fig. S10**), upon heating from -80 °C, first, an endothermic peak is observed at 40 °C (crystalline phase transitions), followed by a large endothermic peak at 130 °C (melting). Also present

is a low enthalpy endothermic peak at 112 °C, possibly indicating the presence of a short-lived crystalline phase. As such, at 24 °C, a crystalline solid is expected, as supported by the XRD pattern which shows characteristic reflections at 11°, 14°, 16°, 19°, 22°, 24° and 25° 20 (blue trace in Fig. 3c(ii)). For the XRD data, as the temperature is increased to 50 °C, new peaks arise adjacent to the features at 19° and 22° 20, corroborating the solid-solid transition observed in DSC. Further heating (up to 115 °C), results in the disappearance of peaks at 11° and 14° 20 as well as the reduction in intensity of peaks at 16°, 19°, 22°, 24° and 25° 20, indicating the onset of a solid-liquid crystalline transition (melting). The XRD pattern at 150 °C (liquid crystalline phase) shows new reflections at 19° and 25° 20 (indicating positional order) along with a broad baseline feature characteristic of pre-melting. These peaks disappear upon further heating, resulting in an XRD pattern with an amorphous halo (isotropic phase) at temperatures above 200 °C. The DSC thermogram of [(EtPFOct)Im][Br] (Fig. S11) displays five endothermic peaks: a large peak at 147 °C (melting) and smaller peaks at 4 °C, 80 °C, 98°C and 120 °C (solid-solid phase transitions). A clearing temperature peak was not observed in the DSC thermogram for this IL, although, this does not exclude the possibility of one occurring at higher temperatures. The DSC thermogram for [(EtPFOct)Im][CI] (Fig. S12) also shows a T_m at 145 °C, in addition to several peaks at lower temperatures possibly arising due to solidsolid phase transitions.

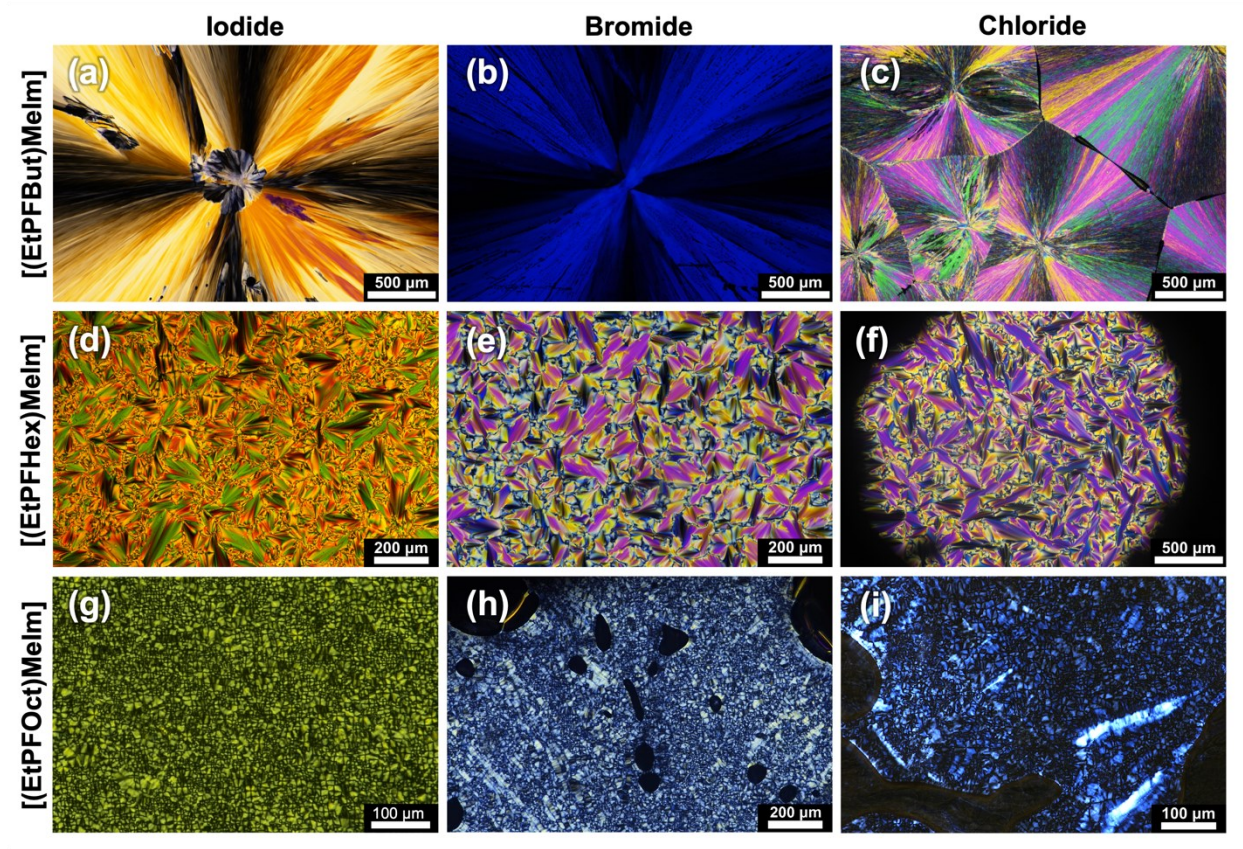


Fig. 4 POM images for [(EtPFBut)Melm] (a) [I] at 24 °C, (b) [Br] at 7 °C, and (c) [CI] at 7 °C. Images for [(EtPFHex)Melm] (d) [I] at 140 °C, (e) [Br] at 150 °C, and (f) [CI] 175 °C. Images for [(EtPFOct)Melm] (g) [I] 190 °C, (h) [Br] 220 °C, and (i) [CI] 200 °C.

3.4 Optical Characterization of the ILs via POM

POM was used to visually confirm mesomorphic behavior for these fluorinated ILs. All samples imaged through POM were heated until isotropic, allowed to cooled to room temperature, then re-heated and recooled. Images were collected in the second cooling cycle at temperatures displaying crystalline/liquid crystalline phases, guided by DSC and XRD data. **Fig. 4** shows POM images taken at various temperatures for the nine ILs discussed herein. The POM image of [(EtPFBut)Im][I] shown in **Fig. 4** reveals a crystalline

phase that forms upon cooling at room temperature and forms a spherulitic structure that appears to have been nucleated from a defect. No other phases were observed at any temperature, thus confirming the previously detailed DSC and XRD data. Likewise, the POM [(EtPFBut)Im][Br] and [(EtPFBut)Im][CI] ILs did not support the presence of LC phases and only revealed a crystalline state at 7 °C, similar to [(EtPFBut)Im][I] as shown in **Fig. 4b** and **Fig. 4c** respectively.

In contrast, all salts containing [(EtPFHex)Im] cation displayed LC phases as seen in Fig. 4d, 4e, and 4f. Upon cooling from the isotropic phase, all three ILs developed aligned domains that appeared as bâtonnets. As the ILs were cooled further, the bâtonnets appeared to grow outward in arcs, simultaneously coalescing, leading to the formation of a focal conic fan texture. The LC phase was assigned as smectic A due to the absence of striations across the fans, as well as a broken fan-shaped texture which would have been present in a smectic C phase.³⁴ Moreover, during the heating cycle of [(EtPFHex)Im][I], an oily streak texture was observed (Fig. S13), which is consistent with a smectic A phase.³⁴ If present, the smectic C phase, on the other hand, would display a schlieren texture.³⁴ The LC phases for all three of these ILs appear around 90-100 °C and remain until the clearing temperature is passed and an isotropic liquid forms, around 220 °C. Fig. 4g, 4h, and 4i represent the LC phases observed for [(EtPFOct)Im] ILs (iodide, bromide, and chloride, respectively), occurring at temperatures exceeding 140 °C. Although a distinct texture is not readily discernible, the LC phase can be characterized as smectic A based on previous reports^{35–37}. Additional support for the identification of the LC phase as smectic A arises from the rarity of smectic C phases in ILCs, particularly those comprised of imidazolium salts. Smectic C phases are typically observed in ILs containing rigid cores or those with alkyl chains containing 7-12 carbon atoms along with C2 methylation.³⁸⁻ ⁴⁰ Thus, the presence of smectic C phases within the ILs examined in this study can be ruled out. Taken together, these data indicate that the fluorinated alkyl chain of the imidazolium cation of the IL must be long enough to impart LC behavior and that the length of the alkyl chain dictates the temperature range that this phase is observed. Notably, the length of these fluorinated alkyl chains that impart ILC behavior (hexyl) is significantly shorter than that previously reported for non-fluorinated chains (undecyl).¹⁵

4. Conclusion

We report the synthesis and characterization of nine different ILs—combinations of three different fluorinated alkyl chain lengths on methylimidazolium cations paired with three different halide anions. Thermal stability and phase transitions were evaluated by TGA and DSC, as well as variable temperature PXRD and POM. Characterization of the ILs by ¹H NMR spectroscopy revealed a clear dependence of the chemical shift of the imidazolium C2-H on the identity of the anion: C2 proton shifts further downfield from CI⁻ to Br⁻ to I⁻. Although this suggests different strength of interactions between the cation and anion, the anion-dependent trends in thermal and optical behavior of ILs were far less discernible. Further characterization of the ILs by TGA revealed no dependence of thermal decomposition temperature of the ILs on the identity of the halide anion nor on the length of the fluorinated chain on the cation.

The identity of the cation appeared to have a profound impact on the thermotropic behavior of ILs. Increasing the length of the fluorinated alkyl chain (i.e., from butyl to hexyl) led to the formation of LC phases, reflecting the lowered degree of localized ordering brought about by the greater rigidity of the longer fluoroalkyl chains. DSC was used in combination with variable temperature PXRD and POM to examine thermotropic phase changes in the samples. ILs with [(EtPFBut)Im] cations showed several solid-solid phase transitions, but did not display any mesomorphic behavior. A LC phase was observed for all salts containing [(EtPFHex)Im] cations at temperatures above 100 °C and those with [(EtPFOct)Im] cations at temperatures above 140 °C, as confirmed through POM. Indeed, increasing the length of the fluorinated chain resulted in the isotropic liquid phase change of ILs being shifted to higher temperatures, affording mesophases present over a wide temperature range. The predominant LC phase across the ILs was identified as smectic A, which is commonly associated with imidazole-based ILs. 30,41,42 In this, the molecules are organized into well-defined layers where the long axes of the molecules are parallel to the director and the layer normal and are stabilized through intermolecular interactions, primarily ionic interactions. These LC phases may indicate these ILs can conduct charge carriers across the mesophase along ordered ion channels, inspiring

their use in energy storage. The fundamental insights from this study unlock a host of opportunities for fluorinated ionic liquids to be used in electrochemical devices such as Li-ion batteries or dye sensitized solar cells.

Author Contributions

R.P. and E.P. designed the experiments. R.P. performed all the synthesis and identity characterization. R.P designed and analyzed TGA and DSC experiments. R.P. and Y.J.L. designed and analyzed POM experiments. R.P. prepared the original draft and all authors reviewed and edited it. T.W. helped analyze data and edit the manuscript. E.P. supervised the project, acquired funding for this research, and edited manuscript.

Conflicts of Interest

There are no conflicts to declare.

Acknowledgements

The authors would like to thank Dr. Anup K. Bandyopadhyay for assisting with the collection of PXRD data. The use of Soft Matter Facility at Texas A&M is also acknowledged. This work is financially supported by National Science Foundation (NSF) award number 2029354 through the Emerging Frontier in Research Innovation (EFRI) DChem program and by award number 2041671 through the Division of Materials Research BIOMAT program.

References

- (1) Liu, Q.; Hsu, C.-W.; Dzwiniel, T. L.; Pupek, K. Z.; Zhang, Z. A Fluorine-Substituted Pyrrolidinium-Based Ionic Liquid for High-Voltage Li-Ion Batteries. *Chem. Commun.* **2020**, *56* (53), 7317–7320. https://doi.org/10.1039/D0CC02184A.
- (2) Li, W.; Pang, Y.; Liu, J.; Liu, G.; Wang, Y.; Xia, Y. A PEO-Based Gel Polymer Electrolyte for Lithium Ion Batteries. *RSC Adv.* **2017**, *7* (38), 23494–23501. https://doi.org/10.1039/C7RA02603J.
- (3) Taghavikish, M.; Subianto, S.; Gu, Y.; Sun, X.; Zhao, X. S.; Choudhury, N. R. A Poly(Ionic Liquid) Gel Electrolyte for Efficient All Solid Electrochemical Double-Layer Capacitor. *Sci. Rep.* **2018**, *8* (1), 10918. https://doi.org/10.1038/s41598-018-29028-y.
- (4) Tiago, G. A. O.; Matias, I. A. S.; Ribeiro, A. P. C.; Martins, L. M. D. R. S. Application of Ionic Liquids in Electrochemistry-Recent Advances. *Molecules* **2020**, *25* (24), E5812. https://doi.org/10.3390/molecules25245812.
- (5) Lei, Z.; Dai, C.; Chen, B. Gas Solubility in Ionic Liquids. *Chem. Rev.* **2014**, *114* (2), 1289–1326. https://doi.org/10.1021/cr300497a.
- (6) Sen, S.; Goodwin, S. E.; Barbará, P. V.; Rance, G. A.; Wales, D.; Cameron, J. M.; Sans, V.; Mamlouk, M.; Scott, K.; Walsh, D. A. Gel–Polymer Electrolytes Based on Poly(Ionic Liquid)/Ionic Liquid Networks. *ACS Appl. Polym. Mater.* **2021**, *3* (1), 200–208. https://doi.org/10.1021/acsapm.0c01042.
- (7) Brutti, S.; Simonetti, E.; De Francesco, M.; Sarra, A.; Paolone, A.; Palumbo, O.; Fantini, S.; Lin, R.; Falgayrat, A.; Choi, H.; Kuenzel, M.; Passerini, S.; Appetecchi, G. B. Ionic Liquid Electrolytes for High-Voltage, Lithium-Ion Batteries. *J. Power Sources* **2020**, *479*, 228791. https://doi.org/10.1016/j.jpowsour.2020.228791.
- (8) Ye, Y.-S.; Rick, J.; Hwang, B.-J. Ionic Liquid Polymer Electrolytes. *J. Mater. Chem. A* **2013**, *1* (8), 2719–2743. https://doi.org/10.1039/C2TA00126H.

- (9) Abu Talip, R. A.; Yahya, W. Z. N.; Bustam, M. A. Ionic Liquids Roles and Perspectives in Electrolyte for Dye-Sensitized Solar Cells. *Sustainability* **2020**, *12* (18), 7598. https://doi.org/10.3390/su12187598.
- (10) Singh, S. K.; Savoy, A. W. Ionic Liquids Synthesis and Applications: An Overview. *J. Mol. Liq.* **2020**, *297*, 112038. https://doi.org/10.1016/j.molliq.2019.112038.
- (11) Gaur, S. S.; Edgehouse, K. J.; Klemm, A.; Wei, P.; Gurkan, B.; Pentzer, E. B. Capsules with Polyurea Shells and Ionic Liquid Cores for CO2 Capture. *J. Polym. Sci* **2021**, *59* (23), 2980–2989. https://doi.org/10.1002/pol.20210342.
- (12) Huang, Q.; Luo, Q.; Wang, Y.; Pentzer, E.; Gurkan, B. Hybrid Ionic Liquid Capsules for Rapid CO2 Capture. *Ind. Eng. Chem. Res.* **2019**, *58* (24), 10503–10509. https://doi.org/10.1021/acs.iecr.9b00314.
- (13) Lee, Y.-Y.; Edgehouse, K.; Klemm, A.; Mao, H.; Pentzer, E.; Gurkan, B. Capsules of Reactive Ionic Liquids for Selective Capture of Carbon Dioxide at Low Concentrations. *ACS Appl. Mater. Interfaces* **2020**, *12* (16), 19184–19193. https://doi.org/10.1021/acsami.0c01622.
- (14) Luo, Q.; Pentzer, E. Encapsulation of Ionic Liquids for Tailored Applications. *ACS Appl. Mater. Interfaces* **2020**, *12* (5), 5169–5176. https://doi.org/10.1021/acsami.9b16546.
- (15) Bowlas, C. J.; Bruce, D. W.; Seddon, K. R. Liquid-Crystalline Ionic Liquids. *Chem. Commun.* **1996**, No. 14, 1625–1626. https://doi.org/10.1039/CC9960001625.
- (16) Holbrey, J. D.; Seddon, K. R. The Phase Behaviour of 1-Alkyl-3-Methylimidazolium Tetrafluoroborates; Ionic Liquids and Ionic Liquid Crystals. *J. Chem. Soc., Dalton Trans.* **1999**, No. 13, 2133–2140. https://doi.org/10.1039/A902818H.
- (17) Gordon, C. M.; Holbrey, J. D.; Kennedy, A. R.; Seddon, K. R. Ionic Liquid Crystals: Hexafluorophosphate Salts. *J. Mater. Chem.* **1998**, *8* (12), 2627–2636. https://doi.org/10.1039/A806169F.
- (18) Bhowmik, P. K.; Noori, O.; Chen, S. L.; Han, H.; Fisch, M. R.; Robb, C. M.; Variyam, A.; Martinez-Felipe, A. Ionic Liquid Crystals: Synthesis and Characterization via NMR, DSC, POM, X-Ray Diffraction and Ionic Conductivity of Asymmetric Viologen Bistriflimide Salts. *J. Mol. Liq.* **2021**, *328*, 115370. https://doi.org/10.1016/j.molliq.2021.115370.
- (19) Goossens, K.; Lava, K.; Bielawski, C. W.; Binnemans, K. Ionic Liquid Crystals: Versatile Materials. *Chem. Rev.* **2016**, *116* (8), 4643–4807. https://doi.org/10.1021/cr400334b.
- (20) Alvarez Fernandez, A.; Kouwer, P. H. J. Key Developments in Ionic Liquid Crystals. *Int. J. Mol. Sci.* **2016**, *17* (5), E731. https://doi.org/10.3390/ijms17050731.
- (21) Yamanaka, N.; Kawano, R.; Kubo, W.; Kitamura, T.; Wada, Y.; Watanabe, M.; Yanagida, S. Ionic Liquid Crystal as a Hole Transport Layer of Dye-Sensitized Solar Cells. *Chem. Commun.* **2005**, *0* (6), 740–742. https://doi.org/10.1039/B417610C.
- (22) Nelyubina, Y. V.; Shaplov, A. S.; Lozinskaya, E. I.; Buzin, M. I.; Vygodskii, Y. S. A New Volume-Based Approach for Predicting Thermophysical Behavior of Ionic Liquids and Ionic Liquid Crystals. *J. Am. Chem. Soc.* **2016**, *138* (32), 10076–10079. https://doi.org/10.1021/jacs.6b05174.
- (23) Downard, A.; Earle, M. J.; Hardacre, C.; McMath, S. E. J.; Nieuwenhuyzen, M.; Teat, S. J. Structural Studies of Crystalline 1-Alkyl-3-Methylimidazolium Chloride Salts. *Chem. Mater.* **2004**, *16* (1), 43–48. https://doi.org/10.1021/cm034344a.
- (24) Vieira, N. S. M.; Ferreira, M. L.; Castro, P. J.; Araújo, J. M. M.; Pereiro, A. B. *Fluorinated Ionic Liquids as Task-Specific Materials: An Overview of Current Research*; IntechOpen, 2021. https://doi.org/10.5772/intechopen.96336.
- (25) Pereiro, A. B.; Araújo, J. M. M.; Martinho, S.; Alves, F.; Nunes, S.; Matias, A.; Duarte, C. M. M.; Rebelo, L. P. N.; Marrucho, I. M. Fluorinated Ionic Liquids: Properties and Applications. *ACS Sustain. Chem. Eng.* **2013**, *1* (4), 427–439. https://doi.org/10.1021/sc300163n.
- (26) Jovell, D.; B. Gómez, S.; Zakrzewska, M. E.; Nunes, A. V. M.; Araújo, J. M. M.; Pereiro, A. B.; Llovell, F. Insight on the Solubility of R134a in Fluorinated Ionic Liquids and Deep Eutectic Solvents. *J. Chem. Eng. Data* **2020**, *65* (10), 4956–4969. https://doi.org/10.1021/acs.jced.0c00588.

- (27) Morais, A. R. C.; Harders, A. N.; Baca, K. R.; Olsen, G. M.; Befort, B. J.; Dowling, A. W.; Maginn, E. J.; Shiflett, M. B. Phase Equilibria, Diffusivities, and Equation of State Modeling of HFC-32 and HFC-125 in Imidazolium-Based Ionic Liquids for the Separation of R-410A. *Ind. Eng. Chem. Res.* **2020**, *59* (40), 18222–18235. https://doi.org/10.1021/acs.iecr.0c02820.
- (28) Shiflett, M. B.; Harmer, M. A.; Junk, C. P.; Yokozeki, A. Solubility and Diffusivity of 1,1,1,2-Tetrafluoroethane in Room-Temperature Ionic Liquids. *Fluid Phase Equilib.* **2006**, *242* (2), 220–232. https://doi.org/10.1016/j.fluid.2006.01.026.
- (29) Shiflett, M. B.; Harmer, M. A.; Junk, C. P.; Yokozeki, A. Solubility and Diffusivity of Difluoromethane in Room-Temperature Ionic Liquids. *J. Chem. Eng. Data* **2006**, *51* (2), 483–495. https://doi.org/10.1021/je050386z.
- (30) Abate, A.; Petrozza, A.; Cavallo, G.; Lanzani, G.; Matteucci, F.; Bruce, D. W.; Houbenov, N.; Metrangolo, P.; Resnati, G. Anisotropic Ionic Conductivity in Fluorinated Ionic Liquid Crystals Suitable for Optoelectronic Applications. *J. Mater. Chem. A* **2013**, *1* (22), 6572–6578. https://doi.org/10.1039/C3TA10990A.
- (31) Zama, I.; Gorni, G.; Borzatta, V.; Cassani, M. C.; Crupi, C.; Di Marco, G. Fluorinated Imidazolium Salts Having Liquid Crystal Characteristics. *J. Mol. Liq.* **2016**, *223*, 749–753. https://doi.org/10.1016/j.molliq.2016.08.101.
- (32) Alcalde, E.; Dinarès, I.; Ibáñez, A.; Mesquida, N. A Simple Halide-to-Anion Exchange Method for Heteroaromatic Salts and Ionic Liquids. *Molecules* **2012**, *17* (4), 4007–4027. https://doi.org/10.3390/molecules17044007.
- (33) Mohammad, A.-T.; Abbas, W. R. Liquid Crystal Behavior, Photoluminescence and Gas Sensing: A New Series of Ionic Liquid Crystal Imidazole and Benzoimidazole Bearing Chalcone Groups, Synthesis and Characterization. *RSC Adv.* **2021**, *11* (61), 38444–38456. https://doi.org/10.1039/D1RA07731G.
- (34) Outram, B. Liquid Crystals; IOP Publishing, 2018.
- (35) Mansueto, M.; Laschat, S. Ionic Liquid Crystals. In *Handbook of Liquid Crystals*; John Wiley & Sons, Ltd, 2014; pp 1–52. https://doi.org/10.1002/9783527671403.hlc095.
- (36) Singh, G.; Kumar, S.; Kang, S.-W. Structures: Liquid Crystals. In *Reference Module in Materials Science and Materials Engineering*; Elsevier, 2016. https://doi.org/10.1016/B978-0-12-803581-8.01257-1.
- (37) Bruce, D. W.; Deschenaux, R.; Donnio, B.; Guillon, D. 12.05 Metallomesogens. In *Comprehensive Organometallic Chemistry III*; Mingos, D. M. P., Crabtree, R. H., Eds.; Elsevier: Oxford, 2007; pp 195–293. https://doi.org/10.1016/B0-08-045047-4/00170-9.
- (38) Renier, O.; Bousrez, G.; Yang, M.; Hölter, M.; Mallick, B.; Smetana, V.; Mudring, A.-V. Developing Design Tools for Introducing and Tuning Structural Order in Ionic Liquids. *CrystEngComm* **2021**, *23* (8), 1785–1795. https://doi.org/10.1039/D0CE01672A.
- (39) Kapernaum, N.; Müller, C.; Moors, S.; Schlick, M. C.; Wuckert, E.; Laschat, S.; Giesselmann, F. First Examples of de Vries-like Smectic A to Smectic C Phase Transitions in Ionic Liquid Crystals. *ChemPhysChem* **2016**, *17* (24), 4116–4123. https://doi.org/10.1002/cphc.201600829.
- (40) Zhang, Q.; Shan, C.; Wang, X.; Chen, L.; Niu, L.; Chen, B. New Ionic Liquid Crystals Based on Azobenzene Moiety with Two Symmetric Imidazolium Ion Group Substituents. *Liquid Crystals* **2008**, *35* (11), 1299–1305. https://doi.org/10.1080/02678290802556211.
- (41) Bousrez, G.; Renier, O.; Adranno, B.; Smetana, V.; Mudring, A.-V. Ionic Liquid-Based Dye-Sensitized Solar Cells—Insights into Electrolyte and Redox Mediator Design. *ACS Sustain. Chem. Eng.* **2021**, *9* (24), 8107–8114. https://doi.org/10.1021/acssuschemeng.1c01057.
- (42) Cavallo, G.; Abate, A.; Rosati, M.; Paolo Venuti, G.; Pilati, T.; Terraneo, G.; Resnati, G.; Metrangolo, P. Tuning of Ionic Liquid Crystal Properties by Combining Halogen Bonding and Fluorous Effect. *ChemPlusChem* **2021**, *86* (3), 469–474. https://doi.org/10.1002/cplu.202100046.

TOC Figure:

